

Correlated Entropic Uncertainty as a Signature of Exceptional Points

Kyu-Won Park,^{1,*} Soojoon Lee,^{1,2} and Kabgyun Jeong^{3,2,†}

¹*Department of Mathematics and Research Institute for Basic Sciences, Kyung Hee University, Seoul, 02447, Korea*

²*School of Computational Sciences, Korea Institute for Advanced Study, Seoul 02455, Korea*

³*Research Institute of Mathematics, Seoul National University, Seoul 08826, Korea*

(Dated: December 23, 2025)

Non-Hermitian physics has become a fundamental framework for understanding open systems where gain and loss play essential roles, with impact across photonics, quantum science, and condensed matter. While the role of complex eigenvalues is well established, the nature of the corresponding eigenfunctions has remained a long-standing problem. Here we show that it arises from a fundamental entropic uncertainty trade-off between phase entropy and its Fourier representation. This trade-off enforces a correlated behavior of phase and Fourier entropies near avoided crossings and exceptional points, precisely where the Petermann factor diverges and phase rigidity collapses. Our results establish biorthogonality is not as an anomaly but an intrinsic property of eigenfunctions, arising universal manifestation of uncertainty relation in non-Hermitian systems. Beyond resolving this foundational question, our framework provides a unifying and testable principle that advances the fundamentals of non-Hermitian physics and can be directly verified with existing interferometric techniques.

PACS numbers:

I. INTRODUCTION

The study of non-Hermitian physics has revealed profound departures from the conventional framework of Hermitian quantum mechanics [1–3]. While the eigenvalues of non-Hermitian Hamiltonians are now well understood—real parts describing energies and imaginary parts associated with gain or loss—the physical nature of the corresponding eigenfunctions remains obscure [4–6]. In Hermitian systems, eigenfunctions form an orthogonal basis, ensuring stability and clarity of interpretation [7]. In contrast, non-Hermitian systems exhibit biorthogonality: right and left eigenfunctions are distinct, and the modes themselves are no longer orthogonal [4, 5, 8]. The fundamental origin of this non-orthogonality, however, has resisted physical explanation [6, 9, 10].

This open question is particularly significant in laser physics, where modal non-orthogonality manifests through the Petermann factor [10–12]. Introduced over three decades ago, the Petermann factor quantifies the excess noise and linewidth broadening of lasers near mode degeneracies [13–15]. Despite its importance, the factor has largely been regarded as a mathematical consequence of biorthogonality rather than the expression of a deeper physical principle [9, 10, 16]. In this sense, the Petermann factor represents both a cornerstone of laser physics and a long-standing puzzle: why does non-orthogonality arise, and what does it physically mean?

Here we propose a new perspective rooted in information theory [17–19]. We analyze the phase distribution of a lasing mode and its Fourier transform, treating them

as conjugate variables in the sense of the entropic uncertainty principle [20–22]. Our analysis reveals that both entropies increase simultaneously near avoided crossings and exceptional points, precisely where modal interactions are strongest [23–25]. Strikingly, the maximum of the total entropic uncertainty coincides exactly with the maximum of the Petermann factor. This establishes that enhanced non-orthogonality is not a mathematical artifact, but rather the physical manifestation of fundamental uncertainty [26–28].

This reinterpretation resolves a decades-old problem by embedding Petermann’s factor into a universal principle: the entropic uncertainty of non-Hermitian modes [11, 26, 27]. In doing so, it elevates biorthogonality from a formal requirement into a physically meaningful property of non-Hermitian eigenfunctions [4, 6, 8]. Beyond resolving a classic issue in laser physics, this framework provides a new tool for understanding and controlling the trade-off between noise and sensitivity in non-Hermitian photonics [1, 29, 30]. More broadly, it opens a pathway toward a universal language for the physical properties of non-Hermitian eigenfunctions, with implications for quantum sensing, open quantum systems, and wave phenomena far beyond optics [2, 3].

II. BACKGROUND

A. Circular statistics for phase fields

Many wave phenomena are most naturally described on the unit circle, where angular observables are periodic and linear averages can be misleading. To summarize such data we employ circular statistics and, in particular, intensity-weighted mean resultants [31–33]. Let a mode

*Electronic address: parkkw7777@gmail.com

†Electronic address: kgjeong6@snu.ac.kr

be written on the interior grid as

$$\psi(\mathbf{r}_j) = r_j e^{i\theta_j} \Rightarrow |\psi(\mathbf{r}_j)|^2 = w_j,$$

where \mathcal{I}_{int} indexes interior grid points (exterior points with $\psi = 0$ are excluded). With weights $w_j = |\psi(\mathbf{r}_j)|^2 = r_j^2$ the k -th mean resultant vector and its mean resultant length (MRL) or are

$$\mathbf{R}_k = \frac{\sum_{j \in \mathcal{I}_{\text{int}}} w_j e^{ik\phi_j}}{\sum_{j \in \mathcal{I}_{\text{int}}} w_j}, \quad R_k = |\mathbf{R}_k| \in [0, 1].$$

We emphasize that it is the MRL R_k (the modulus of the weighted mean resultant), not the complex vector \mathbf{R}_k , that is invariant under an additive global phase shift. Indeed, under $\phi_j \mapsto \phi_j + c$ one has $\mathbf{R}_k \mapsto e^{ikc} \mathbf{R}_k$, hence

$$R'_k = |\mathbf{R}'_k| = |e^{ikc}| |\mathbf{R}_k| = R_k.$$

The quantity R_k therefore measures concentration of the angle $k\phi$ on the unit circle: $R_k \approx 1$ indicates strong concentration (which can be interpreted as circular coherence or phase) of $k\phi$, while $R_k \approx 0$ indicates dispersion or cancellation. In this work we will use R_2 specifically to quantify π -periodic concentration of the phase field – i.e. the degree to which ϕ and $\phi + \pi$ are indistinguishable in the weighted sample – and R_1 to detect imbalance between opposite directions (sign imbalance between phases separated by π). Further physical interpretations (for example those referring to Hermitian vs non-Hermitian behaviour and to ‘0/ π locking’) are deferred to the sections that treat Hermitian and non-Hermitian settings explicitly.

B. Phase rigidity: from biorthogonal eigenmodes to spatial measures and the Petermann factor

Open systems with leakage, absorption, or gain are conveniently described by non-Hermitian operators H , whose right and left eigenmodes form biorthogonal pairs [4, 5, 8].

$$H |\psi_k^R\rangle = E_k |\psi_k^R\rangle, \quad \langle \psi_k^L | H = E_k \langle \psi_k^L |. \quad (1)$$

Biorthogonality implies $\langle \psi_m^L | \psi_n^R \rangle = 0$ for $m \neq n$, but in general $\langle \psi_k^L | \psi_k^R \rangle \neq 1$. A convenient, normalization-independent scalar measure of modal non-orthogonality (often called the *phase rigidity* or overlap) is

$$\tilde{r}_k = \frac{|\langle \psi_k^L | \psi_k^R \rangle|}{\sqrt{\langle \psi_k^R | \psi_k^R \rangle \langle \psi_k^L | \psi_k^L \rangle}} \in [0, 1]. \quad (2)$$

By construction \tilde{r}_k is invariant under arbitrary rescaling of the left and right eigenvectors and hence provides a model-independent indicator of how close a mode is to being self-orthogonal ($\tilde{r}_k \rightarrow 0$) or perfectly biorthogonal ($\tilde{r}_k \rightarrow 1$).

The Petermann factor K_k – originally introduced in laser theory to quantify excess spontaneous-emission noise beyond the Schawlow–Townes limit – can be written in terms of left/right norms and their overlap as [11–13].

$$K_k = \frac{\langle \psi_k^R | \psi_k^R \rangle \langle \psi_k^L | \psi_k^L \rangle}{|\langle \psi_k^L | \psi_k^R \rangle|^2}. \quad (3)$$

Combining (2) and (3) yields the simple and frequently used relation

$$K_k = \frac{1}{\tilde{r}_k^2}. \quad (4)$$

Thus, a collapse of \tilde{r}_k directly produces a growth (and in the limit a divergence) of K_k . Physically, this relation explains why strong modal non-orthogonality amplifies spontaneous-emission-induced noise and increases the quantum-limited laser linewidth. In practice one often writes

$$\Delta\nu \approx K_k \Delta\nu_{\text{ST}},$$

where $\Delta\nu_{\text{ST}}$ is the Schawlow–Townes linewidth.

The extreme behaviour of \tilde{r}_k and K_k typically occurs near exceptional points or under strong resonance overlap: left and right eigenvectors become nearly linearly dependent, $\tilde{r}_k \rightarrow 0$ and K_k grows large, with the concomitant trade-off of enhanced responsivity but degraded coherence. For this reason, mapping \tilde{r}_k (or K_k) across relevant parameter ranges is essential for understanding and controlling noise-sensitivity trade-offs. In the commonly used complex-symmetric case ($H^T = H$) the left mode is proportional to the transpose of the right mode (up to a scalar), which considerably simplifies numerical evaluation on the spatial grid.

III. SPECTRAL AND MODAL COMPARISON BETWEEN CLOSED AND OPEN ELLIPTIC CAVITIES

Figure 1(a) presents the real parts of the eigenvalues, $\text{Re}(k)$, for the closed elliptic billiard (the integrable, Hermitian limit) as the shape parameter ϵ is varied. In this integrable case the two levels approach and undergo a *simple crossing* near $\epsilon \approx 0.16$ [23]. Because the governing operator is Hermitian and the two branches carry distinct quantum numbers or symmetry labels, no hybridization occurs at the intersection and each branch preserves its modal identity. The adjacent eigenmode visualizations labelled A–F display the standing-wave real-amplitude patterns associated with each branch and emphasize well-formed nodal structure and strict parity/phase locking rather than any exchange of spatial structure.

Figure 1(b) shows the corresponding behaviour for the open (non-Hermitian) elliptic cavity. Radiation loss and coupling to the continuum render the effective operator

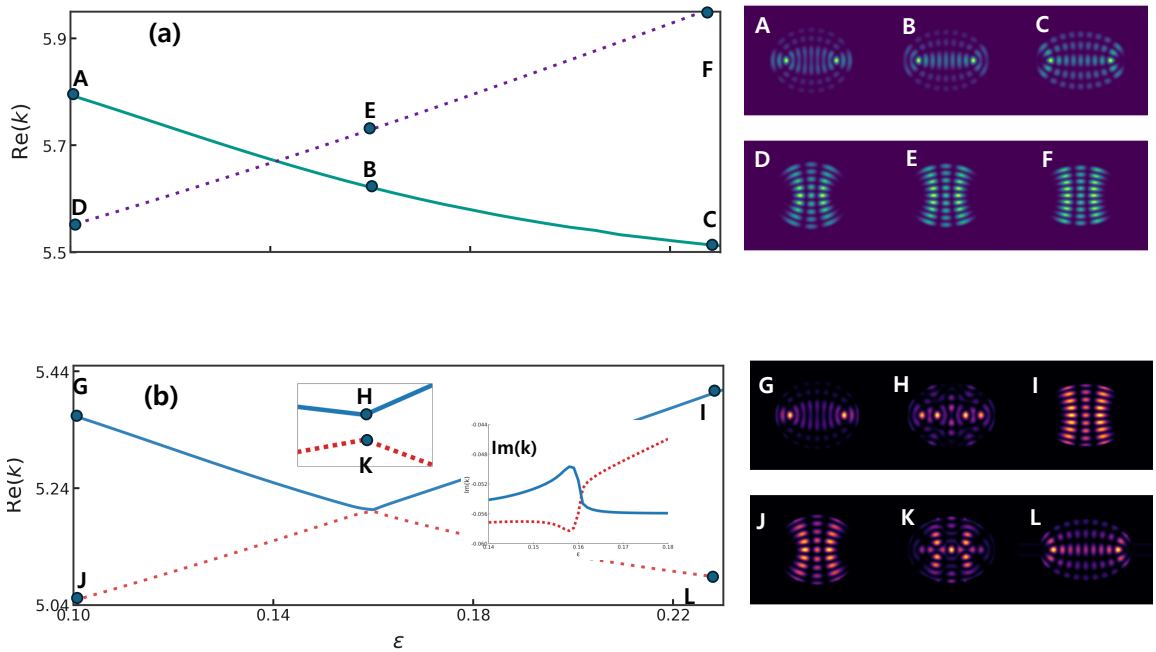


FIG. 1: (a) Real parts of the eigenvalues $\text{Re}(k)$ for the closed (integrable, Hermitian) elliptic billiard. The two indicated levels intersect in a simple crossing near $\epsilon \approx 0.16$; representative eigenmodes A–F (right) show the standing-wave real-amplitude patterns on each branch and confirm the absence of hybridization. (b) The corresponding open (non-Hermitian) elliptic cavity: $\text{Re}(k)$ now displays an avoided crossing (A.C.) near the same ϵ value. The central inset magnifies the avoided-crossing region to show the characteristic spectral repulsion in $\text{Re}(k)$, while the side inset plots the imaginary parts $\text{Im}(k)$ and reveals a true crossing of the decay rates (complementary motion in the complex eigenplane). Eigenmodes G–L (right) illustrate the structural exchange across the A.C.: modal intensity is transferred between branches as the pair hybridizes.

non-Hermitian, and the same nominal level pair exhibits an *avoided crossing* (A.C.) in $\text{Re}(k)$ near the same value of ϵ [5, 24, 34]. The central inset magnifies the avoided-crossing region and makes the spectral repulsion in the real parts explicit; the side inset plots the imaginary parts, $\text{Im}(k)$, and demonstrates that while the real parts repel the decay rates cross – a signature behaviour of non-Hermitian mode interaction in the complex eigenplane. The eigenmodes G–L illustrate a clear structural exchange across the A.C.: following the continuous evolution through the avoided crossing, modal intensity patterns transfer from one branch to the other, indicating hybridization and identity exchange in the open system. These contrasting panels underline the qualitative difference between Hermitian level crossings (no hybridization) and non-Hermitian avoided crossings (mode mixing), and they motivate the subsequent analysis of phase patterns and entropy diagnostics for the same modes.

IV. PHASE MAPS: HERMITIAN LOCKING VS NON-HERMITIAN DELOCALIZATION

To examine the spatial phase properties of each computed eigenmode we express the field in complex (polar) form, thereby separating local amplitude and phase. This representation isolates the pointwise phase for di-

rect visualization and later circular-consistent comparisons. Specifically, write the complex eigenmode in polar form at each point,

$$\psi(\mathbf{r}) = A(\mathbf{r}) e^{i\phi(\mathbf{r})}, \quad A(\mathbf{r}) \geq 0,$$

and compute the phase as $\phi = \text{atan2}(\Im\psi, \Re\psi)$, which takes values in the principal interval $(-\pi, \pi]$. Because π and $-\pi$ represent the same physical angle, all histogramming, binning and angular comparisons are performed circularly: histograms are constructed on $(-\pi, \pi]$ with wrap-around between the first and last bins, and any angular difference is reduced to its principal (shortest) value. In particular we define the circular angular difference relative to a reference angle ϕ_0 by

$$\Delta(\phi, \phi_0) = \text{angle_wrap}(\phi - \phi_0) \in (-\pi, \pi],$$

where `angle_wrap` denotes reduction to the principal value in $(-\pi, \pi]$. In practice we choose $\phi_0 \in \{0, \pi, -\pi\}$ when assessing locking to those canonical peaks; using $\Delta(\phi, \phi_0)$ therefore allows a circularly consistent assessment of how close each sample is to a given locking angle and facilitates visualization of whether the phase mass remains concentrated at the peaks or has diffused away.

These definitions connect simply to the real (Hermitian) limit: if $\psi(\mathbf{r}) \in \mathbb{R}$ then $\phi(\mathbf{r}) \in \{0, \pi\} \pmod{2\pi}$: positive real values give $\phi = 0$, negative real values give

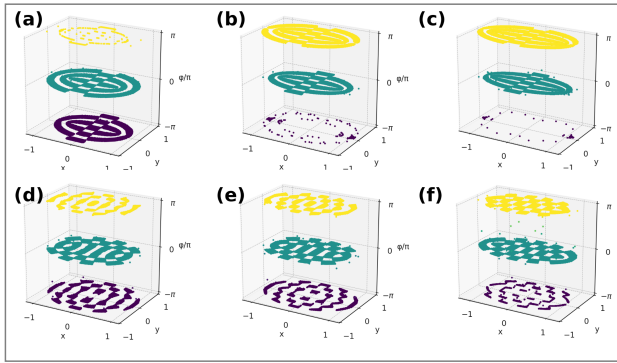


FIG. 2: Phase maps shown as 3D point clouds in $(x, y, \phi/\pi)$; color encodes ϕ/π (viridis), duplicating the vertical coordinate for visual emphasis. (a)–(f) Closed (Hermitian) elliptic cavity: the phase collapses to the planes $\phi/\pi \in \{0, \pm\pi\}$, consistent with standing-wave parity and strong phase locking. (g)–(l) Corresponding open (non-Hermitian) modes: the phase values diffuse away from the locked planes at 0 and $\pm\pi$, indicating partial delocalization that weakens phase locking and reduces phase rigidity relative to the closed case. Panels (a)–(l) follow the same mode ordering as Fig. 1 (A–F for the closed case and G–L for the open case).

$\phi = \pi$ (or $-\pi$). Conversely, $\phi \in \{0, \pi\}$ implies $\psi = \pm A$ is real. Note that $\phi = \pi$ does *not* require a nonzero imaginary part (for example $-2 = 2e^{i\pi}$ is purely real and negative). At nodes ($A = 0$) the phase is undefined; such points are excluded or heavily down-weighted in practice because they carry negligible probability density [35–37].

Figure 2 directly illustrates the central observation: closed (Hermitian) modes show tight phase locking at 0 and $\pm\pi$, whereas the corresponding open (non-Hermitian) modes display a clear broadening away from those peaks. The contrast has a simple origin in boundary-domain symmetry. In closed cavities with real coefficients and real boundary conditions (e.g. Dirichlet or Neumann), complex conjugation K leaves both the bulk operator and its domain invariant, so one has the true commutation relation $[H, K] = 0$ and eigenmodes may be chosen real. By contrast, for open (radiative) boundary conditions the domain is not invariant under K (or time reversal T): T (or K) maps outgoing to in-

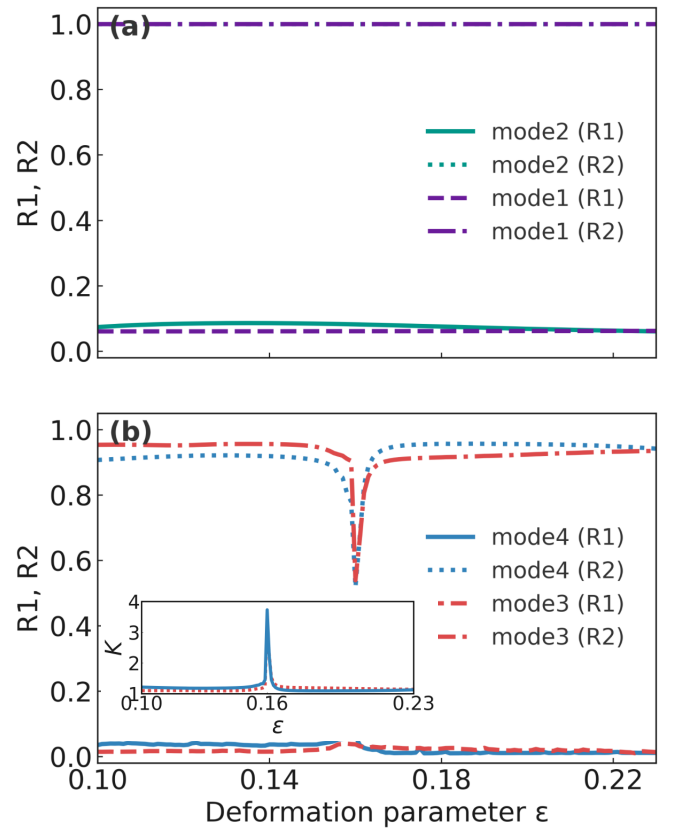


FIG. 3: (a) R_1 and R_2 for the closed-ellipse (Hermitian) modes (mode1: $k \approx 5.44$, mode2: $k \approx 5.92$). (b) R_1 and R_2 for the open-ellipse (non-Hermitian) modes (mode4: $k \approx 5.49$, mode3: $k \approx 4.96$). R_1 and R_2 are the first and second resultant lengths computed from phase distributions weighted by $|\psi|^2$ (see Methods). Data are shown as a function of the deformation parameter $\varepsilon \in [0.10, 0.23]$. The avoided crossing (A.C.) near $\varepsilon \approx 0.16$ in the open system produces the characteristic dip in R_2 and an accompanying response in R_1 .

coming conditions, so that $TH_{\text{out}}T^{-1} = H_{\text{in}} \neq H_{\text{out}}$. The commonly written relation $\Psi(t) = \Phi^*(-t)$ therefore expresses a mapping between right (outgoing) and left (incoming) solutions rather than a symmetry of a single operator-with-domain; consequently, eigenmodes need not be real and non-Hermitian phenomena (including exceptional points and the accompanying phase delocalization) are fully consistent with this setting [4, 5, 34].

V. MEAN RESULTANT LENGTH AND PETERMANN FACTOR

a. Standing waves and current. A real-valued eigenmode may be written as $\psi(\mathbf{r}) = A(\mathbf{r})e^{i\phi(\mathbf{r})}$ with $\phi(\mathbf{r}) \in \{0, \pi\}$ almost everywhere (away from nodal lines). The probability/energy current

$$\mathbf{j}(\mathbf{r}) = \Im(\psi^* \nabla \psi) = A^2(\mathbf{r}) \nabla \phi(\mathbf{r})$$

vanishes for a globally real mode ($\nabla\phi = 0 \implies \mathbf{j} \equiv 0$). Hence equal total areas of the $+/$ lobes are *not* required for a standing wave; sizeable lobe imbalance can coexist with $\mathbf{j} \equiv 0$. Apparent tiny currents near nodal lines in finite-difference computations reflect discretization rather than a failure of the analytical statement [7].

b. Circular moments (mean resultant lengths). To quantify phase binarity and lobe imbalance we use intensity-weighted circular moments

$$R_k \equiv |\langle e^{ik\phi} \rangle_w|, \quad w := |\psi|^2.$$

A distribution concentrated at $\phi \approx 0, \pi$ gives $e^{i2\phi} \approx 1$ and thus $R_2 \simeq 1$. Writing the $+$ and $-$ phase weights as

$$W_+ := \sum_{\cos \phi_j > 0} w_j, \quad W_- := \sum_{\cos \phi_j < 0} w_j,$$

the ideal two-valued case $\phi \in \{0, \pi\}$ yields

$$R_1 = \frac{|W_+ - W_-|}{W_+ + W_-},$$

so R_1 quantifies the *weight imbalance* of the two lobes, whereas R_2 measures the *binarity* at $0/\pi$. Importantly, $R_1 > 0$ does not imply $\mathbf{j} \neq 0$; the current is governed by phase gradients rather than lobe weights [31–33].

Given interior grid samples $\{\psi_j\}$ we form weights $w_j := |\psi_j|^2$ and principal phases

$$\phi_j = (\text{atan2}(\Im \psi_j, \Re \psi_j) + 2\pi) \bmod 2\pi.$$

Since atan2 returns angles in $(-\pi, \pi]$, we add 2π and reduce modulo 2π to map values consistently into $[0, 2\pi)$; this avoids the spurious wraparound that would occur if only π were added.

In general complex eigenfunctions admit a continuous global phase factor $e^{i\phi} \in U(1)$. Under the reality condition this continuous symmetry collapses to the discrete subgroup $\mathbb{Z}_2 = \{0, \pi\}$, reflecting the fact that only a global sign matters. To quantify deviations from perfect reality we further identify this \mathbb{Z}_2 as trivial by introducing the doubling map

$$D : \mathbb{T}^{(\phi)} \rightarrow \mathbb{T}^{(\theta)}, \quad D([\phi]) = [2\phi] \pmod{2\pi}.$$

This map is a continuous surjective group homomorphism with kernel $\ker D = \{[0], [\pi]\} \cong \mathbb{Z}_2$, so that the reduction chain

$$U(1) \longrightarrow \mathbb{Z}_2 \xrightarrow{D} \{0\}$$

is realized. Consequently, any strictly real mode with $\phi_j \in \{0, \pi\}$ is sent to the identity $\theta_j = 0$ in $\mathbb{T}^{(\theta)}$, and the folded distribution is the Dirac mass at the identity, $p_\theta = \delta_0$. In this baseline, the first resultant length

$$R_1^{(\theta)} = \left| \frac{1}{\sum_j w_j} \sum_j w_j e^{i\theta_j} \right| = 1$$

is maximized.

Departures from reality (nonzero imaginary parts, non-Hermitian mixing, avoided-crossing neighborhoods) spread ϕ_j away from $\{0, \pi\}$, so that $\theta_j = 2\phi_j$ cluster near but not exactly at zero. This yields a reduction $0 < R_1^{(\theta)} < 1$. Equivalently, in the original ϕ -space one may write

$$R_2^{(\phi)} = \left| \frac{1}{\sum_j w_j} \sum_j w_j e^{2i\phi_j} \right| = R_1^{(\theta)}.$$

Thus $R_1^{(\theta)}$ provides a group-theoretic measure of how far the folded distribution lies from the identity element of the additive circle $\mathbb{T}^{(\theta)}$. In other words, $R_1^{(\theta)}$ quantifies the distance from the trivial subgroup $\{0\}$, thereby capturing the transition from real (Hermitian) to genuinely complex (non-Hermitian) eigenfunctions.

c. Numerical procedure (rotation-invariant alignment). Given interior grid samples $\{\psi_j\}$ we form $w_j := |\psi_j|^2$ and principal phases

$$\phi_j := (\text{atan2}(\Im \psi_j, \Re \psi_j) + 2\pi) \bmod 2\pi.$$

Because the eigenmodes are defined only up to an overall sign, the phases are π -periodic. To respect this two-fold symmetry we work with the doubled angle variable $\theta_j = 2\phi_j$, which is 2π -periodic and admits a conventional circular statistics treatment. We then compute the second-harmonic resultant

$$Z_2 = \sum_j w_j e^{i\theta_j}, \quad \mu_2 := \arg Z_2,$$

and align the phases by

$$\theta_j^{(\text{shift})} = (\theta_j - \mu_2 + \frac{\Delta}{2}) \bmod 2\pi, \quad \Delta = \frac{2\pi}{N_{\text{bins}}}.$$

The half-bin offset centers the representative direction and mitigates edge-splitting. This alignment is rotation-invariant: for $\theta'_j = \theta_j + 2\alpha$ one has $Z'_2 = e^{2i\alpha} Z_2$ and thus $\theta_j^{(\text{shift})} = \theta'_j$. After alignment the phase distribution can be written compactly as

$$p_\theta(\theta) = \frac{1}{\sum_j w_j} \sum_j w_j \delta(\theta - (2\phi_j \bmod 2\pi)),$$

where the weights are $w_j = |\psi(\mathbf{r}_j)|^2$.

Conceptually, this distribution is nothing but the push-forward of the original phase distribution p_ϕ under the doubling map $D : \phi \mapsto \theta = 2\phi \pmod{2\pi}$, which in density form reads

$$p_\theta(\theta) = \frac{1}{2} \left(p_\phi\left(\frac{\theta}{2}\right) + p_\phi\left(\frac{\theta}{2} + \pi\right) \right).$$

In practice, the continuous distribution $p_\theta(\theta)$ is approximated by a discrete probability mass function obtained through histogramming. Specifically, the interval $[0, 2\pi]$ is subdivided into $N_{\text{bins}} = 720$ bins of equal width

$\Delta\theta = 2\pi/N_{\text{bins}}$. For each bin b , we accumulate the total weight

$$h_b = \sum_{\theta_j \in \text{bin } b} w_j,$$

which represents the unnormalized bin mass. The corresponding normalized probability mass function is then defined as

$$p_b = \frac{h_b}{\sum_j w_j}, \quad \sum_{b=0}^{N_{\text{bins}}-1} p_b = 1.$$

Given interior grid samples $\{\psi_j\}$ we form $w_j := |\psi_j|^2$ and principal phases

$$\phi_j := (\text{atan2}(\Im\psi_j, \Re\psi_j) + 2\pi) \bmod 2\pi.$$

Because the eigenmodes are defined only up to an overall sign, the phases are π -periodic. To respect this two-fold symmetry we work with the doubled angle variable $\theta_j = 2\phi_j$, which is 2π -periodic and admits a conventional circular statistics treatment. We then compute the second-harmonic resultant

$$Z_2 = \sum_j w_j e^{i\theta_j}, \quad \mu_2 := \arg Z_2,$$

and align the phases by

$$\theta_j^{(\text{shift})} = (\theta_j - \mu_2 + \frac{\Delta}{2}) \bmod 2\pi, \quad \Delta = \frac{2\pi}{N_{\text{bins}}}.$$

The half-bin offset centers the representative direction and mitigates edge-splitting. This alignment is rotation-invariant: for $\theta'_j = \theta_j + 2\alpha$ one has $Z'_2 = e^{2i\alpha} Z_2$ and thus $\theta_j'^{(\text{shift})} = \theta_j^{(\text{shift})}$. After alignment the phase distribution can be written compactly as

$$p_\theta(\theta) = \frac{1}{\sum_j w_j} \sum_j w_j \delta(\theta - (2\phi_j \bmod 2\pi)).$$

where the weights are $w_j = |\psi(\mathbf{r}_j)|^2$. In practice, the continuous distribution $p_\theta(\theta)$ is approximated by a discrete probability mass function obtained through histogramming. Specifically, the interval $[0, 2\pi)$ is subdivided into $N_{\text{bins}} = 720$ bins of equal width $\Delta\theta = 2\pi/N_{\text{bins}}$. For each bin b , we accumulate the total weight

$$h_b = \sum_{\theta_j \in \text{bin } b} w_j,$$

which represents the unnormalized bin mass. The corresponding normalized probability mass function is then defined as

$$p_b = \frac{h_b}{\sum_j w_j}, \quad \sum_{b=0}^{N_{\text{bins}}-1} p_b = 1.$$

Results. In the closed ellipse (panel a), both modes remain nearly binary in phase: $R_2 \approx 1$ for all ε , while $R_1 \approx 0$ (raw offsets $< 10^{-3}$ set to zero), consistent with self-adjoint real-coefficient operators for which nondegenerate eigenmodes are globally real. In the open ellipse (panel b), the A.C. at $\varepsilon \approx 0.16$ produces a sharp *dip* in R_2 , indicating a collapse of 2ϕ -coherence (phase delocalization away from $0/\pi$); a smaller but noticeable response appears in R_1 due to changing lobe weights. Away from the A.C., $R_2 \rightarrow 1$ as the modes restabilize.

d. Cartesian viewpoint and limiting cases. Write $\psi_k = u_k + iv_k$ with real u_k, v_k . In the complex-symmetric setting ($H^T = H$) the (complex) phase rigidity can be expressed as the normalized overlap

$$\tilde{r}_k = \frac{\int_{\Omega} \psi_k^2 d\mathbf{r}}{\int_{\Omega} |\psi_k|^2 d\mathbf{r}} = \frac{\int_{\Omega} (u_k^2 - v_k^2) d\mathbf{r} + 2i \int_{\Omega} u_k v_k d\mathbf{r}}{\int_{\Omega} (u_k^2 + v_k^2) d\mathbf{r}}.$$

Two immediate sanity checks follow: if the mode is globally real ($v_k \equiv 0$), then $|\tilde{r}_k| = 1$, while as the imaginary part grows and reaches that of the real part (with the cross-term removed by the aligned gauge) $|\tilde{r}_k|$ decreases continuously to 0 (the real \rightarrow imaginary transition).

e. Equivalence to R_2 and Petermann. Noting $\psi_k^2 = |\psi_k|^2 e^{2i\phi}$, the numerator above equals the weighted second circular moment, hence

$$|\tilde{r}_k| = R_2[\psi_k],$$

and under the complex-symmetric assumption the Petermann factor reduces to

$$K_k = \frac{1}{|\tilde{r}_k|^2} = \frac{1}{(R_2[\psi_k])^2}.$$

This mapping is monotone on $R_2 \in (0, 1]$ (so $R_2 = 1 \Rightarrow K = 1$, $R_2 \rightarrow 0 \Rightarrow K \rightarrow \infty$) and satisfies $\frac{dK}{dR_2} = -2\frac{dR_2}{R_2^2}$, so fractional changes are linked: a given relative decrease of R_2 produces roughly twice that relative increase in K . Furthermore, R_2 is invariant under global phase rotations and normalized by total intensity, it provides a compact, gauge-independent phase-statistical proxy for modal non-orthogonality in this setting [9, 11, 12].

VI. PHASE ENTROPY

In conventional Hermitian settings, the physical content of an eigenmode is largely captured by its intensity, since $|\psi|^2$ directly represents probability/energy density; the phase can be flattened by a single global gauge and typically leaves no independent signature. By opening the cavity or introducing non-Hermitian terms, this picture changes qualitatively: the phase field becomes spatially delocalized twisting and spreading in ways no single gauge can undo. As a result, the phase entropy S_ϕ

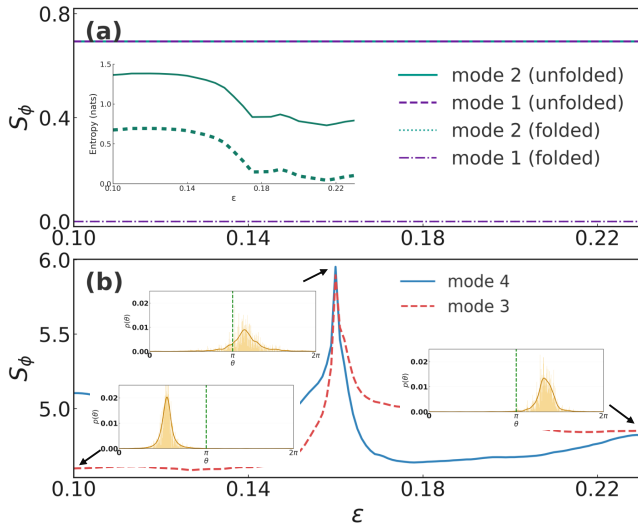


FIG. 4: Phase entropy S_ϕ across an avoided crossing. (a) *Hermitian* (closed) modes (1,2): solid/dashed curves are the *unfolded* estimator, dotted/dash-dot curves are the *folded* estimator (histogrammed in $\theta = 2\phi$). The inset shows the same traces computed *without* the μ_2 -alignment, illustrating edge-splitting artefacts. (b) *Non-Hermitian* (open) modes (3,4): both modes display a sharp maximum of S_ϕ at the A.C. center ($\epsilon \approx 0.1666$), signalling strong phase delocalization that coincides with the Petermann-factor spike discussed in the text. Entropies were computed from intensity-weighted histograms; values are reported in nats.

emerges as a highly sensitive marker of non-Hermitian behavior, peaking near A.C. and tracking both the loss of phase rigidity r and the growth of the Petermann factor K . The figure below leverages this sensitivity by quantifying non-Hermitian deformation via S_ϕ along the control parameter ϵ .

The preceding section established the relevance of the circular moments R_1, R_2 and the empirical link between a collapse of R_2 and Petermann growth (Sec. V). To probe whether Petermann increases near avoided crossings arise from true phase delocalization (rather than a mere redistribution of intensity between two π -locked lobes) we adopt the Shannon phase entropy as an information-theoretic diagnostic as follows: Note that a continuous (differential) circular entropy is manifestly invariant under a global phase shift: if $H_c = - \int_0^{2\pi} f(\phi) \ln f(\phi) d\phi$ and $f_\alpha(\phi) = f(\phi - \alpha)$ then the substitution $\phi' = \phi - \alpha$ yields $H_c[f_\alpha] = H_c[f]$. By contrast, a raw histogram on fixed bins is sensitive to rigid rotations (samples can cross bin boundaries); hence we employ the 2ϕ -alignment procedure of Sec. V so that the discrete (histogram) entropy is comparable across modes.

For this, We define the phase-entropy as a functional on the space of probability measures over the folded circle,

$$S_\theta : \mathcal{P}(\mathbb{T}^{(\theta)}) \longrightarrow \mathbb{R},$$

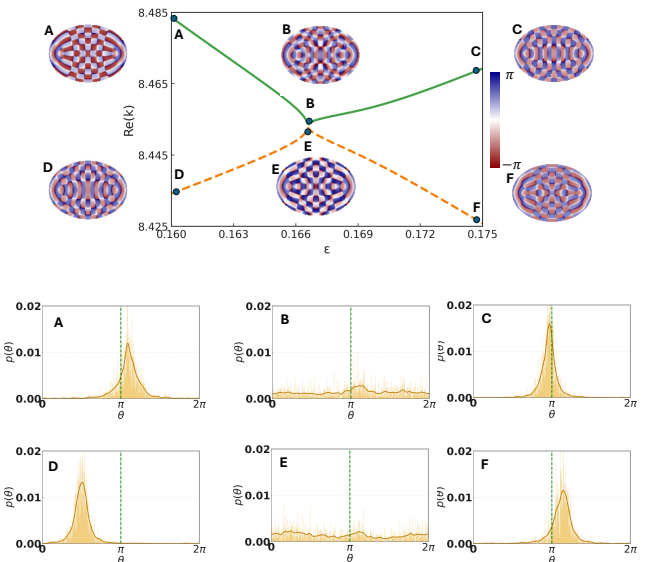


FIG. 5: (a) Avoided crossing of modes 5 and 6 very near an exceptional point; panels A–F show representative interior phase maps (A: pre–A.C., F: post–A.C.; exact ϵ values are indicated on the panels). (b) Petermann factor K (solid lines, left axis) and phase entropy S_ϕ (dashed lines, right axis) for the same modes; both quantities peak at the A.C.

where $\mathcal{P}(\mathbb{T}^{(\theta)})$ denotes the space of all Borel probability measures on the compact topological group $\mathbb{T}^{(\theta)} = \mathbb{R}/2\pi\mathbb{Z}$. In other words, each $p_\theta \in \mathcal{P}(\mathbb{T}^{(\theta)})$ is a countably additive probability measure with $p_\theta(\mathbb{T}^{(\theta)}) = 1$.

If p_θ admits a density $p_\theta(\theta)$ with respect to the Lebesgue measure on $[0, 2\pi]$ (so that $\int_0^{2\pi} p_\theta(\theta) d\theta = 1$), the Shannon entropy is defined by [17, 19].

$$S_\theta(p_\theta) = - \int_0^{2\pi} p_\theta(\theta) \log p_\theta(\theta) d\theta,$$

where \log denotes the natural logarithm.

For a discretization into N_{bins} equal bins with probability masses $\{p_b\}_{b=1}^{N_{\text{bins}}}$, one uses the empirical approximation

$$S_\theta^{(\text{disc})} = - \sum_{b=1}^{N_{\text{bins}}} p_b \log p_b, \quad \sum_{b=1}^{N_{\text{bins}}} p_b = 1.$$

Figure 4 compares the closed (Hermitian) case [panel (a), modes 1-2] with its open non-Hermitian counterpart [panel (b), modes 3-4]. For each mode we compute the phase entropy S_ϕ from intensity-weighted phases after alignment by the 2ϕ resultant; both the unfolded estimator (phases shifted by $\arg Z_2/2$) and the folded estimator (histogrammed in $\theta = 2\phi$) are shown. In the closed system the eigenmodes remain π -locked over the sweep, and both estimators yield a low, nearly flat baseline of S_ϕ . The inset in panel (a) repeats the calculation *without* alignment and exhibits artificial edge-splitting in the his-

togram, explaining the small residual offsets removed by our alignment/half-bin procedure.

In the ideal Hermitian limit ($R_2 \approx 1$ and $R_1 \approx 0$) the unfolded estimator attains the two-point value $S_\phi \approx \ln 2$ (≈ 0.693 nats), while the folded estimator is (ideally) $S_\phi \approx 0$.

In contrast, the open system displays a sharply localized maximum of S_ϕ at the avoided-crossing center ($\varepsilon \approx 0.1666$) for both modes 3 and 4, signaling strong phase delocalization caused by modal hybridization. The peak position coincides with the minimum of R_2 and hence with the Petermann-factor spike via $K = 1/R_2^2$, linking nonorthogonality growth to the collapse of the 2ϕ coherence.

We interpret the phase histogram $p(\theta)$, normalized over $[0, 2\pi]$, as a probability density in angle space. Its Fourier coefficients are defined as

$$F_k = \int_0^{2\pi} p(\theta) e^{-ik\theta} d\theta \approx \frac{1}{\sum_j w_j} \sum_j w_j e^{-ik\theta_j}, \quad (5)$$

with weights $w_j = |\psi_j|^2$ and principal phases θ_j . Within circular-statistics terminology, the intensity-weighted mean resultants are then identified as

$$\mathbf{R}_k = F_{-k}, \quad R_k = |F_k|,$$

so that the mean resultant length R_k coincides with the magnitude of the k th Fourier coefficient. In particular, the first Fourier component F_1 (equivalently R_1) quantifies the strength of two fold phase alignment, which, as we show below, directly governs the Petermann factor and thereby measures modal non-orthogonality. Normalizing the absolute values $|F_k|$ yields a probability distribution over the Fourier mode index k , providing a representation in the *value space*. Here the value space refers to the set of actual values taken by the random variable $X(k) = |F_k|$ with $k \in \mathbb{Z}$, i.e. the collection $\{|F_k| : k \in \mathbb{Z}\} \subset \mathbb{R}_{\geq 0}$. Since $\sum_k |F_k|$ is finite in practice, these amplitudes can be normalized to unity, thereby endowing the value space with a probability measure and placing the Fourier side on the same probabilistic footing as the phase-space distribution $p(\theta)$.

$$\text{θ-space: } p(\theta) \longleftrightarrow \text{k-space: } |F_k|.$$

This duality naturally invites entropic measures. The variance product $\Delta\phi \Delta k$ encodes the conventional trade-off: reduced spread in one domain enforces increased spread in the other. In contrast, the entropic uncertainty relation,

$$S_\phi + S_{|k|} \geq \log(\pi e), \quad (6)$$

provides a universal lower bound on the *total* delocalization across both domains, capturing the full global structure of the distributions rather than just local variance.

Figure 6 illustrates these concepts near the avoided crossing that hosts an exceptional point (EP). Panels (A–F) show the Fourier spectra $|F_k|$ of the representative eigenmodes from Fig. 5, truncated at $k = 50$. As $\varepsilon \rightarrow \varepsilon_{EP}$, the overall magnitude of the coefficients is strongly suppressed, signaling delocalization in Fourier space.

Panels (a–c) directly compare entropic and non-orthogonality measures. Panel (a) displays the Petermann factor κ (left axis) alongside the phase entropy S_ϕ (right axis) for modes 5 and 6, both exhibiting sharp peaks at $\varepsilon \approx \varepsilon_{EP}$. Panels (b) and (c) show the entropic uncertainty sum $S_\phi + S_{|k|}$ for modes 5 and 6, respectively, with insets resolving the separate contributions S_ϕ and $S_{|k|}$. In each case both entropies rise together and reach their maxima *simultaneously* at the EP.

In stark contrast to the standard uncertainty principle where one entropy increases only at the expense of the other, here all entropic measures *coincide in growth* [26, 27, 38]. The simultaneous maximization of phase entropy, Fourier entropy, their sum, and the Petermann factor,

$$\arg \max_{\varepsilon} \{\kappa, S_\phi, S_{|k|}, S_\phi + S_{|k|}\} = \varepsilon_{EP},$$

establishes the EP as a universal organizing center where Fourier suppression, entropic delocalization, and modal non-orthogonality converge. To resolve the apparent coincidence of the peaks of the phase entropy S_ϕ and the Fourier entropy S_K , we introduce the notion of Rényi entropy [19, 28, 39]. The Rényi- α entropy of a discrete phase distribution $p = \{p_n\}_{n=0}^{N-1}$ is defined by

$$H_\alpha(p) = \frac{1}{1-\alpha} \log \sum_{n=0}^{N-1} p_n^\alpha. \quad (7)$$

This one-parameter family not only interpolates smoothly between quadratic and Shannon cases, but also provides an exact identity at $\alpha = 2$ that links entropy maximization to the suppression of non-DC Fourier energy. The continuity in α then ensures that the observed maxima of S_ϕ and S_K are structurally enforced to coincide rather than being accidental.

More precisely, Rényi entropy can be expressed as a Rényi divergence from the uniform distribution $u_n = 1/N$:

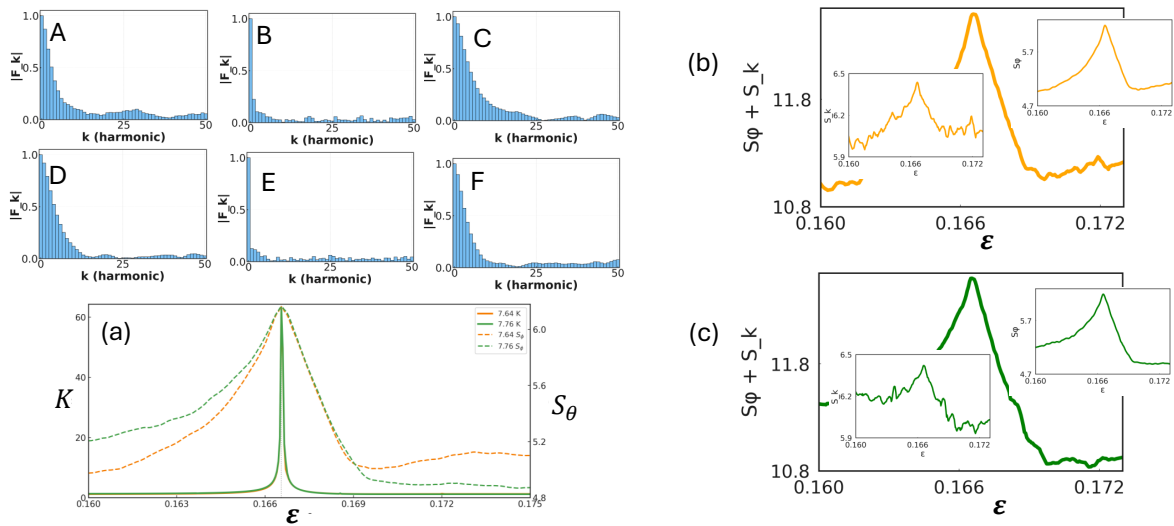


FIG. 6: Fourier spectra and entropic measures near an exceptional point (EP). (A–F) show the Fourier coefficients $|F_k|$ of the representative eigenmodes in Fig. 5, truncated at $k = 50$. As $\varepsilon \rightarrow \varepsilon_{EP}$ the overall magnitude of the coefficients is strongly suppressed, reflecting the delocalization of the Fourier spectrum. (a) Petermann factor κ (left axis) and phase entropy S_ϕ (right axis) for modes 5 and 6, both peaking simultaneously at $\varepsilon \approx \varepsilon_{EP}$. (b) Entropic uncertainty $S_\phi + S_{|k|}$ for mode 5, again exhibiting a maximum at $\varepsilon \approx \varepsilon_{EP}$; insets display the separate contributions S_ϕ and $S_{|k|}$. (c) Same as (b), but for mode 6. Together these results demonstrate that all entropic peaks are fixed at the EP, i.e. $\arg \max_\varepsilon \{S_\phi, S_{|k|}, S_\phi + S_{|k|}\} = \varepsilon_{EP}$, highlighting $\varepsilon \approx \varepsilon_{EP}$ as a universal organizing center for Fourier suppression, Petermann divergence, and entropic uncertainty.

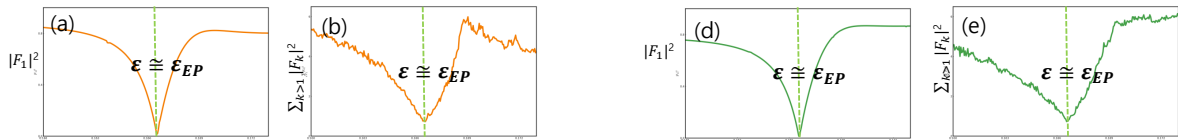


FIG. 7: Fourier components and Rényi entropy near an exceptional point (EP). For mode 5 (a–c) and mode 6 (d–f), the three panels display in sequence: the squared magnitude of the first Fourier coefficient $|F_1|^2$, the cumulative contribution of the higher-order components $\sum_{k>1} |F_k|^2$, and the Rényi entropy H_α for $\alpha = 2 \rightarrow 1$. Vertical dashed lines mark the EP position ($\varepsilon \approx \varepsilon_{EP}$), serving as a common reference across all panels. Of particular importance, the entropy peaks highlighted by red dashed lines in (c,f) are not free to shift arbitrarily but remain locked to $\varepsilon \approx \varepsilon_{EP}$, demonstrating that the maxima of H_α coincide robustly with the EP itself. This coincidence underscores the physical role of EPs as organizing centers for both Fourier weight redistribution and correlated entropic growth.

$$H_\alpha(p) = \log N - D_\alpha(p\|u), \quad D_\alpha(p\|q) = \frac{1}{\alpha-1} \log \sum_n p_n^\alpha q_n^{1-\alpha}, \quad (8)$$

which reduces to the Kullback–Leibler divergence in the limit $\alpha \rightarrow 1$. Thus, Rényi entropy quantifies the information-theoretic distance of p from equipartition.

For the quadratic case $\alpha = 2$, Parseval’s theorem directly connects the phase distribution and its Fourier representation:

$$\sum_k |F_k|^2 = N \sum_n p_n^2. \quad (9)$$

That is, the second-order moment of the phase distribution is encoded in the total Fourier energy.

Substituting this relation into the definition of H_2 gives

$$H_2(p) = \log N - \log(1 + \chi^2(p)), \quad (10)$$

where $\chi^2(p) = \sum_{k \geq 1} |F_k|^2$ denotes the non-DC Fourier energy. In this form, entropy maximization corresponds to the vanishing of spectral weight away from $k = 0$, i.e. the approach of p to uniformity. Thus the maximum of H_2 coincides with the minimum of the Fourier energy, providing a rigorous spectral signature of maximal entropy.

Since the Rényi entropies are continuous and monotonically decreasing in α , the peak of H_2 persists under the deformation $\alpha : 2 \rightarrow 1$, converging smoothly to the Shannon entropy H . This continuity ensures that entropy maximization is not a fragile effect of a specific choice of α but a structurally enforced feature of the distribution.

Let $p_b = 1/N + \delta_b$ with $\sum_b \delta_b = 0$, and define $y_b := N\delta_b$, so that

$$p_b = \frac{1}{N}(1 + y_b), \quad \sum_b y_b = 0.$$

A Taylor expansion around the uniform distribution gives

$$H_1 = \log N - \frac{1}{2}N \sum_b \delta_b^2 + \frac{1}{6}N^2 \sum_b \delta_b^3 + O(\|\delta\|^4), \quad (11)$$

so that $H_1 \approx \log N - \frac{1}{2}\chi^2$ with $\chi^2 = N \sum_b \delta_b^2$. In our data ($N = 720$ bins, peak entropy $H_1 \approx 6.22$ versus the uniform maximum $\log N \approx 6.579$), the gap $\Delta H \approx 0.359$ implies $\chi^2 \approx 0.718$ and hence $\sum_b \delta_b^2 \approx 9.98 \times 10^{-4}$, corresponding to $\|\delta\|_2 \approx 3.16$. For comparison, in the extreme case of a delta distribution where all weight is concentrated in a single bin, one has $\delta_b = 1 - 1/N$ for one bin and $-1/N$ for the others, yielding $\|\delta\|_2 \approx 1$; hence our value $\|\delta\|_2 \approx 0.0316$ is indeed very small.

This confirms that the distribution is indeed close to uniform, making the quadratic Taylor expansion quantitatively reliable. Formally, the peak condition is given by

$\Phi(\varepsilon, \alpha) = \partial_\varepsilon H_\alpha(\varepsilon) = 0$. At $(\varepsilon_\star \cong \varepsilon_{EP}, 2)$ this holds with $\partial_\varepsilon \Phi \neq 0$, so by the implicit function theorem there exists a unique smooth branch $\varepsilon(\alpha)$ solving $\Phi(\varepsilon(\alpha), \alpha) = 0$. Hence the entropy maximum moves continuously as α varies, rather than jumping discontinuously.

Hence both are strictly decreasing functions of $\chi^2(\varepsilon)$ and their maxima are pinned to the same parameter value ε^* where χ^2 attains its minimum. Together these arguments show that the maxima of H_α for $\alpha \in [1, 2]$ are not free to drift but remain locked to the avoided-crossing parameter ε^* .

Figure 7 illustrates these relations for modes 5 and 6. For each mode the three panels (a–c) and (d–f) show in sequence: (i) the squared magnitude of the first Fourier coefficient $|F_1|^2$, (ii) the cumulative contribution of higher-order components $\sum_{k>1} |F_k|^2$, and (iii) the Rényi entropy H_α for $\alpha = 2 \rightarrow 1$. Vertical dashed lines mark the EP position ($\varepsilon \approx \varepsilon_{EP}$), serving as a common reference across all panels. Of particular importance, the entropy peaks highlighted by red dashed lines in (c,f) are not free to shift arbitrarily but remain locked to $\varepsilon \approx \varepsilon_{EP}$.

Consequently, the simultaneous growth of the phase entropy $H(\theta)$ and the Fourier entropy $H(k)$ near avoided crossings is not an incidental feature but a structural necessity: spectral suppression in Fourier space enforces both entropies to peak at the same control parameter. In this way, the exceptional point is revealed not merely as a spectral singularity but as a *universal information-theoretic attractor*—a locus where Fourier weight redistribution, entropic enhancement, and modal non-orthogonality are locked together. This perspective elevates EPs from mathematical curiosities to organizing centers that govern the joint statistical and spectral complexity of non-Hermitian eigenmodes.

VII. CONCLUSION

We have shown that modal non-orthogonality, quantified by the Petermann factor, originates from a fundamental increase in entropic uncertainty [11, 12, 22]. In non-Hermitian systems, the simultaneous growth of phase and Fourier entropies near avoided crossings and exceptional points marks the transition from ordered to disordered modal structures. This directly explains why the Petermann factor peaks in such regimes: it is the physical fingerprint of enhanced uncertainty.

This insight elevates biorthogonality from a mathematical necessity to a physically interpretable property of non-Hermitian eigenfunctions. By embedding Petermann’s factor into the framework of information the-

ory, we not only resolve a long-standing problem in laser physics but also establish a universal tool to quantify noise-sensitivity trade-offs in non-Hermitian photonics. We anticipate that this perspective will extend to other wave systems—from quantum sensing to condensed matter and biological networks—where non-Hermitian physics governs critical behavior.

VIII. ACKNOWLEDGEMENT

This work was supported by the National Research Foundation of Korea (NRF) through a grant funded by

the Ministry of Science and ICT (Grants Nos. RS2023-00211817 and RS-2025-00515537), the Institute for Information & Communications Technology Promotion (IITP) grant funded by the Korean government (MSIP) (Grants Nos. RS-2019-II190003 and RS-2025-02304540), the National Research Council of Science & Technology (NST) (Grant No. GTL25011-000), and the Korea Institute of Science and Technology Information (KISTI). S.L. acknowledges support from the National Research Foundation of Korea (NRF) grants funded by the MSIT (Grant No. RS-2022-NR068791)

[1] R. El-Ganainy, K. G. Makris, M. Khajavikhan, Z. H. Musslimani, S. Rotter, and D. N. Christodoulides, Non-Hermitian physics and PT symmetry, *Nat. Phys.* **14**, 11–19 (2018).

[2] Y. Ashida, Z. Gong, and M. Ueda, Non-Hermitian physics, *Adv. Phys.* **69**, 249–435 (2020).

[3] E. J. Bergholtz, J. C. Budich, and F. K. Kunst, Exceptional topology of non-Hermitian systems, *Rev. Mod. Phys.* **93**, 015005 (2021).

[4] N. Moiseyev, *Non-Hermitian Quantum Mechanics* (Cambridge University Press, Cambridge, 2011).

[5] I. Rotter, A non-Hermitian Hamilton operator and the physics of open quantum systems, *J. Phys. A: Math. Theor.* **42**, 153001 (2009).

[6] L. N. Trefethen and M. Embree, *Spectra and Pseudospectra: The Behavior of Nonnormal Matrices and Operators* (Princeton University Press, Princeton, 2005).

[7] J. J. Sakurai and J. Napolitano, *Modern Quantum Mechanics*, 2nd ed. (Cambridge University Press, Cambridge, 2017).

[8] T. Kato, *Perturbation Theory for Linear Operators* (Springer, Berlin, 1995).

[9] A. E. Siegman, Excess spontaneous emission in non-Hermitian optical systems. I. Laser amplifiers, *Phys. Rev. A* **39**, 1253–1263 (1989).

[10] M. V. Berry, Mode degeneracies and the Petermann excess-noise factor for unstable lasers, *J. Mod. Opt.* **50**, 63–81 (2003).

[11] K. Petermann, Calculated spontaneous emission factor for double-heterostructure injection lasers with gain-induced waveguiding, *IEEE J. Quantum Electron.* **QE-15**, 566–570 (1979).

[12] A. E. Siegman, Excess spontaneous emission in non-Hermitian optical systems. II. Laser oscillators, *Phys. Rev. A* **39**, 1264–1271 (1989).

[13] A. L. Schawlow and C. H. Townes, Infrared and optical masers, *Phys. Rev.* **112**, 1940–1949 (1958).

[14] C. H. Henry, Theory of the linewidth of semiconductor lasers, *IEEE J. Quantum Electron.* **QE-18**, 259–264 (1982).

[15] Y. D. Chong, L. Ge, H. Cao, and A. D. Stone, General linewidth formula for steady-state multimode lasing in arbitrary cavities, *Phys. Rev. Lett.* **109**, 063902 (2012).

[16] H. Schomerus, K. M. Frahm, M. Patra, and C. W. J. Beenakker, Quantum limit of the laser linewidth in chaotic cavities and statistics of residues of scattering matrix poles, *Physica A* **278**, 469–496 (2000).

[17] C. E. Shannon, A mathematical theory of communication, *Bell Syst. Tech. J.* **27**, 379–423 and 623–656 (1948).

[18] E. T. Jaynes, Information theory and statistical mechanics, *Phys. Rev.* **106**, 620–630 (1957).

[19] T. M. Cover and J. A. Thomas, *Elements of Information Theory*, 2nd ed. (Wiley, New York, 2006).

[20] I. I. Hirschman, Jr., A note on entropy, *Amer. J. Math.* **79**, 152–156 (1957).

[21] W. Beckner, Inequalities in Fourier analysis, *Ann. Math.* **102**, 159–182 (1975).

[22] I. Bialynicki-Birula and J. Mycielski, Uncertainty relations for information entropy in wave mechanics, *Commun. Math. Phys.* **44**, 129–132 (1975).

[23] J. von Neumann and E. Wigner, Über merkwürdige diskrete Eigenwerte, *Phys. Z.* **30**, 465 (1929).

[24] W. D. Heiss, The physics of exceptional points, *J. Phys. A: Math. Theor.* **45**, 444016 (2012).

[25] C. Dembowski, H.-D. Gräf, H. L. Harney, A. Heine, W. D. Heiss, H. Rehfeld, and A. Richter, Experimental observation of the topological structure of exceptional points, *Phys. Rev. Lett.* **86**, 787–790 (2001).

[26] S. Wehner and A. Winter, Entropic uncertainty relations: a survey, *New J. Phys.* **12**, 025009 (2010).

[27] P. J. Coles, M. Berta, M. Tomamichel, and S. Wehner, Entropic uncertainty relations and their applications, *Rev. Mod. Phys.* **89**, 015002 (2017).

[28] I. Bialynicki-Birula, Formulation of the uncertainty relations in terms of the Rényi entropies, *Phys. Rev. A* **74**, 052101 (2006).

[29] M.-A. Miri and A. Alù, Exceptional points in optics and photonics, *Science* **363**, eaar7709 (2019).

[30] S. K. Ozdemir, S. Rotter, F. Nori, and L. Yang, Parity-time symmetry and exceptional points in photonics, *Nat. Mater.* **18**, 783–798 (2019).

[31] N. I. Fisher, *Statistical Analysis of Circular Data* (Cambridge University Press, Cambridge, 1993).

[32] K. V. Mardia and P. E. Jupp, *Directional Statistics* (Wiley, New York, 2000).

[33] S. R. Jammalamadaka and A. Sengupta, *Topics in Circular Statistics* (World Scientific, Singapore, 2001).

[34] H. Cao and J. Wiersig, Dielectric microcavities: model systems for wave chaos and non-Hermitian physics, *Rev. Mod. Phys.* **87**, 61–111 (2015).

- [35] J. F. Nye and M. V. Berry, Dislocations in wave trains, *Proc. R. Soc. Lond. A* **336**, 165–190 (1974).
- [36] M. V. Berry and M. R. Dennis, Phase singularities in isotropic random waves, *Proc. R. Soc. Lond. A* **456**, 2059–2079 (2000).
- [37] M. R. Dennis, K. O'Holleran, and M. J. Padgett, Singular optics: optical vortices and polarization singularities, in *Progress in Optics*, Vol. 53, pp. 293–363 (Elsevier, 2009).
- [38] D. Deutsch, Uncertainty in quantum measurements, *Phys. Rev. Lett.* **50**, 631–633 (1983).
- [39] A. Rényi, On measures of entropy and information, in *Proceedings of the Fourth Berkeley Symposium on Mathematical Statistics and Probability*, Vol. 1, pp. 547–561 (University of California Press, Berkeley, 1961).